SCIENTIFIC REPORTS
natureresearch

OPEN

Photovoltaic and flexible deep ultraviolet wavelength detector based on novel β-Ga_2O_3/muscovite heteroepitaxy

Bhera Ram Tak[1]✉, Ming-Min Yang[2], Yu-Hong Lai[3], Ying-Hao Chu[3], Marin Alexe[2] & Rajendra Singh[1]

Flexible and self-powered deep ultraviolet (UV) photodetectors are pivotal for next-generation electronic skins to enrich human life quality. The fabrication of epitaxial β-Ga_2O_3 thin films is challenging on flexible substrates due to high-temperature growth requirements. Herein, β-Ga_2O_3 ($\bar{2}$ 0 1) films are hetero-epitaxially grown on ultra-thin and environment-friendly muscovite mica which is the first time β-Ga_2O_3 epitaxy growth on any flexible substrate. Integration of Gallium oxide with muscovite enables high-temperature processing as well as excellent flexibility compared to polymer substrates. Additionally, the metal–semiconductor-metal (MSM) photodetector on β-Ga_2O_3 layer shows an ultra-low dark current of 800 fA at zero bias. The photovoltaic peak responsivity of 11.6 μA/W is obtained corresponding to very weak illumination of 75 μW/cm^2 of 265 nm wavelength. Thermally stimulated current (TSC) measurements are employed to investigate the optically active trap states. Among these traps, trap with an activation energy of 166 meV dominates the persistence photocurrent in the devices. Finally, photovoltaic detectors have shown excellent photocurrent stability under bending induced stress up to 0.32%. Hence, this novel heteroepitaxy opens the new way for flexible deep UV photodetectors.

Flexible electronics with smart materials are playing a key role to meet market demands of future technologies. Internet of things (IoT), wearable electronics, healthcare and electronic skins (e-skins) are major driving application areas for futuristic smart or flexible devices[1,2]. Along with aforementioned research directions, flexible devices like transistors, photodetectors, memristors, displays and sensors are prerequisite for smart electronics[3–10]. Due to these vast application areas, the global flexible electronics market is expected to grow at about 10.5% growth rate till 2026[11]. In the era of robotics, flexible e-skin with various sensors such as optical, pressure, chemical sensors, etc. will necessitate to function it like human's skin. E-skin with UV photodetectors can enhance the visuals by imaging which can also act as the electronic eye (e-eye) as well as the second skin[12]. Among the wide spectrum of UV radiation, deep UV (< 280 nm) wavelength is most energetic and dangerous for living beings[13]. This wavelength spectrum is almost completely absorbed by the ozone layer. Therefore, photodetectors working in deep UV range possess negligible background signals at the earth's surface. Deep UV photodetectors also important in emerging applications such as space communications, water disinfection, defense, environmental monitoring etc.[14–16].

The future of flexible electronics also poses various challenges such as providing integrated power sources, temperature harsh fabrication processing for good quality crystalline materials, and also being environment friendly in nature[17,18]. Power consumption is a serious issue to harvest these flexible photodetectors. Usage of power sources with flexible photodetectors makes them bulky and complex when the requirement of many more sensors on the same platform will occur. Specifically, advanced e-skin photodetectors require elimination of power supply requirements[19]. Therefore, photovoltaic detectors are of vital importance for e-skins. In case of photovoltaic operation, photo-generated charge carriers are collected using built-in electric field at the electrode terminals rather than external applied electric field. The built-in electric field in p–n junction develops at the

[1]Department of Physics, Indian Institute of Technology, Delhi, New Delhi 110016, India. [2]Department of Physics, University of Warwick, Coventry CV4 7AL, UK. [3]Department of Materials Science and Engineering, National Chiao Tung University, Hsinchu 30010, Taiwan. ✉email: bheraramtak@gmail.com

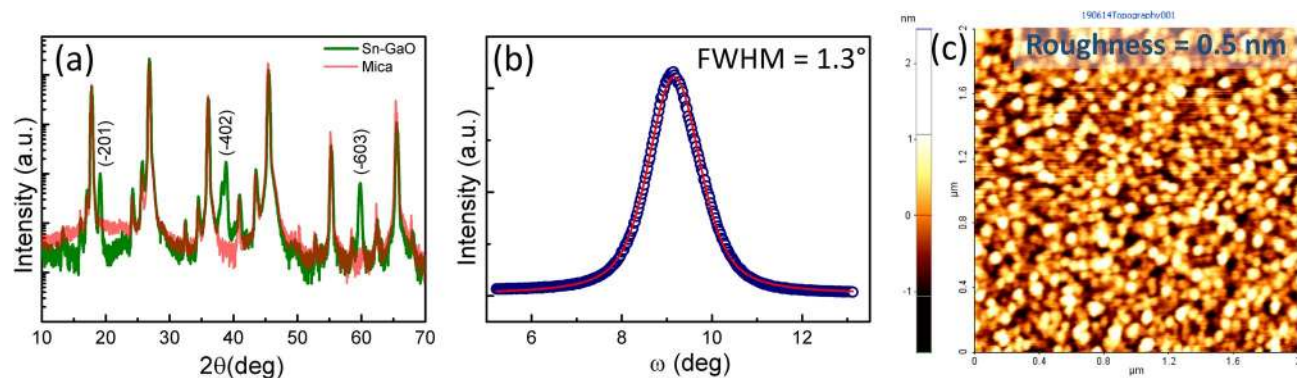

Figure 1. (**a**) XRD 2θ-scan of β-Ga_2O_3/muscovite, (**b**) rocking curve of $(\bar{2}01)$-plane and (**c**) surface morphology of β-Ga_2O_3 thin film.

depletion region due to opposite polarity of semiconductor materials as well as band offsets (for heterojunctions)[20] whereas in Schottky diodes, the built-in electric field exists at the metal–semiconductor junction.

Nowadays, most of the flexible UV photodetectors are fabricated on polymer substrates such as PET, PDMS, and PEN[21–23]. Generally, devices fabricated on epitaxial materials exhibit better performance than amorphous materials. However, the fabrication of epitaxial thin films on flexible substrates is impossible due to the degradation of these substrates at high-temperatures as required for the epitaxial growth. Muscovite mica is a natural substrate that can resolve both the aforementioned challenges of high-temperature processing and environment friendliness[24]. The muscovite has high-temperature stability up to 650 °C. Ultra-thin mica substrate with few nanometer thickness have been reported[25]. The thickness of flexible substrates must be less than 100 µm to function as an e-skin[26]. Therefore, mica is also a strong contender for e-skins. Moreover, muscovite owes superior Young's modulus, thermal conductivity, and tensile strength than polymer substrates such as PET, PDMS, PEN, etc[24]. Being two-dimensional (2D) and layered substrate, the surface of muscovite is free from the dangling bonds. According to Koma et al., the thin film growth progresses on 2D materials with weak interactions rather than strong chemical bonding between thin film and substrate[27,28]. Thus, the growth method is called as van der Waals epitaxy. Even with large lattice mismatch, van der Waals epitaxy growth mechanism provides the excellent heteroepitaxial growth. Earlier, many high-quality functional oxides such as Fe_2O_3, MoO_2, VO_2, yttria-stabilized zirconia (YSZ), $CoFe_2O_4$ have been epitaxially grown on muscovite mica. These functional oxides had lattice mismatch with muscovite ranging from 8 to 36% but it didn't affect the material quality due to van der Waals epitaxy growth[29–33].

Nowadays, Ga_2O_3 and AlGaN are the most widely used wide bandgap semiconductors for deep UV photodetector applications[14,34–41]. Recently, Ga_2O_3 has emerged as a better candidate than AlGaN due to its intrinsic deep UV absorption which eliminates the complexity of heavy doping[42]. Only a few research works are performed on the growth of gallium oxide thin films on flexible substrates. Thin films used in these reports were amorphous[23,43]. So far, the epitaxial deposition of β-Ga_2O_3 thin films on flexible substrates has been a major challenge. To fill this research gap, self-powered and flexible deep UV photodetectors based on epitaxial β-Ga_2O_3 thin films are reported here. The optically active trap states have also been identified, which contribute towards the persistent photocurrent observed in the devices.

Results and discussion

To begin with, structural properties of the Ga_2O_3 thin film are investigated by high-resolution X-ray diffraction (HRXRD). Out of plane X-ray 2θ scan of Ga_2O_3/muscovite heterostructure is shown in Fig. 1(a). The red color plot depicts the diffraction pattern of muscovite whereas the green color plot represents the diffraction pattern of Ga_2O_3/muscovite heterostructure. It shows that $(\bar{2}\ 0\ 1)$ orientation (JCPDS No.-431012) of monoclinic β-Ga_2O_3 was grown on muscovite. Moreover, phi (ϕ)-scan of β-Ga_2O_3 $(\bar{4}\ 0\ 1)$ diffraction is recorded for in-plane structural correlation which is shown in Figure S1. Six peaks are observed in the ϕ-scan of $(\bar{4}\ 0\ 1)$ plane at the interval of 60°. The $(\bar{4}\ 0\ 1)$ reflection plane of β-Ga_2O_3 possesses two-fold symmetry. Therefore, observation of six peaks in the ϕ-scan represents the three-fold domains in the β-Ga_2O_3 epitaxy. Furthermore, the crystalline quality of the thin film is analyzed using the rocking curve measurement of $(\bar{2}\ 0\ 1)$ plane giving full width at half maximum (FWHM) of 1.3° as depicted in Fig. 1(b). This FWHM of β-Ga_2O_3 epitaxy is much lower than the reported MBE grown thin films (1.38–1.99°)[44,45]. HRXRD reveals the epitaxial relationship between β-Ga_2O_3 and mica as $(\bar{2}\ 0\ 1)$ Ga_2O_3/(001)Mica. Figure 1(c) shows the surface topography of thin film recorded by atomic force microscopy in $2 \times 2\ \mu m^2$ scan area. The root mean square roughness of 0.5 nm is obtained which revealed that the thin film is quite smooth and can be used for device fabrications.

To further confirm the epitaxial relationship and interfacial characterization, a cross-sectional imaging of the β-Ga_2O_3/mica interface is done using a high-resolution transmission microscope (HRTEM) and is shown in Fig. 2(a). The sharp interface between Ga_2O_3 thin film and mica is also indicated in Fig. 2(a). The fast Fourier transforms (FFT) of the Ga_2O_3 thin film and mica in the reciprocal space are indicated in Fig. 2(b,c) simultaneously. The FFT images also confirm the epitaxial relationship as β-Ga_2O_3 $(\bar{2}\ 0\ 1)$/mica (0 0 1).

Further, photoelectrical characterization of the metal–semiconductor–metal photodetector fabricated using heteroepitaxial films is carried out. The current–voltage (I–V) characteristics are measured under dark and

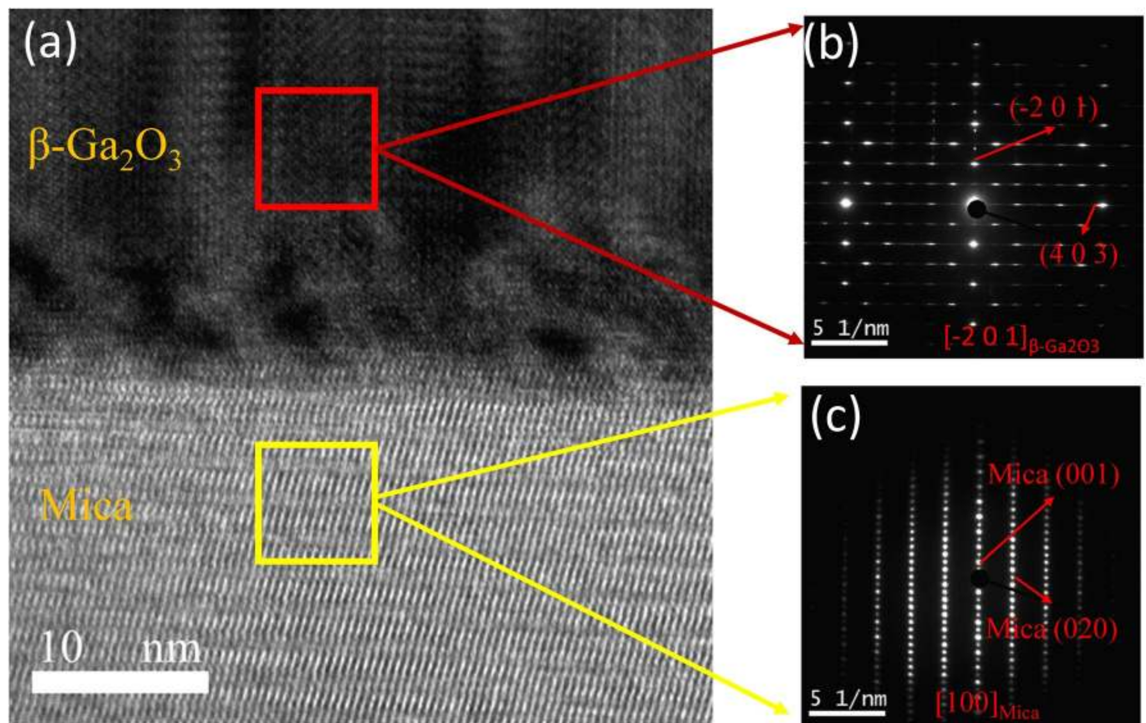

Figure 2. (**a**) Cross-sectional TEM image of β-Ga_2O_3/muscovite mica interface, (**b**) SAED pattern of β-Ga_2O_3 thin film and (**c**) SAED pattern of muscovite mica.

265 nm illumination, as shown in Fig. 3(a). The photocurrent is 45 times larger than the dark current. Here photovoltaic response i.e. zero bias photoresponse is also noticed under illumination, which is known as a self-powered behaviour in photodetectors. This self-powered behaviour is advantageous for the sensors in terms of power consumption which is the need of the current technology. The responsivity of a photodetector is defined as[14,46]

$$R = \frac{I_p - I_d}{P_\lambda \times A} \tag{1}$$

where I_d and I_p denote dark and photocurrent respectively. P_λ represents the power density at wavelength λ and A is the effective area of the device under illumination. The voltage-dependent peak responsivity under 265 nm illumination is shown in Fig. 3(b). The zero-bias peak responsivity of 11.6 μA/W was obtained at a weak power density of 75 μW/cm^2.

For a better performance evaluation of the current work, photovoltaic UV-C detectors are compared in Table 1 with different device architectures. The epitaxial growth of β-Ga_2O_3 is also compared due to importance of channel layer in the photodetector performance. Thus, low temperature grown β-Ga_2O_3/muscovite heterostructures provided UV-C photovoltaic detector with simple MSM architecture and ultra-low dark current. Flexibility of Ga_2O_3/muscovite heterostructure is another important merit over reported photovoltaic UV-C wavelength detectors.

Further, the photovoltaic current obtained under the illumination of 265 nm wavelength is displayed in Fig. 3(c). The photocurrent increases/decreases exponentially with time during switching on/off the illumination. It is observed that photocurrent persisted for several seconds after switching off the illumination. The photocurrent rise and decay curves can be fitted with biexponential Eq. 2 and 3, respectively:[14,23,40]

$$I = I_s + Ae^{t/\tau_{r1}} + Be^{/\tau_{r2}} \tag{2}$$

$$I = I_s + Ae^{t/\tau_{d1}} + Be^{t/\tau_{d2}} \tag{3}$$

where I_s represents the steady-state current and A and B are the fitting constants. τ_{r1} and τ_{r2} are fast and slow components of rise times whereas τ_{d1} and τ_{d2} denote the fast and slow components of decay times. Two rise/decay times are obtained by fitting of time response curve using Eqs. (2) and (3). The rise times τ_{r1} and τ_{r2} of 1.78 s and 14.80 s are obtained whereas the decay times of 2.09 s and 33.06 s are acquired. The slow component of rise/decay time is attributed to charge carrier trapping/de-trapping owing to the presence of bandgap states. Larger values of slow components represent the persistent photocurrent in the detector. In this case, high persistent photocurrent is obtained in the time response curve due to the existence of bandgap states in the β-Ga_2O_3 films. These trap levels may get charged due to trapping of carriers generated by light.

In order to confirm the existence of defects in the bandgap as well as to identify the peak responsivity, we performed spectral response measurements. The normalized spectral responsivity of the fabricated photodetector

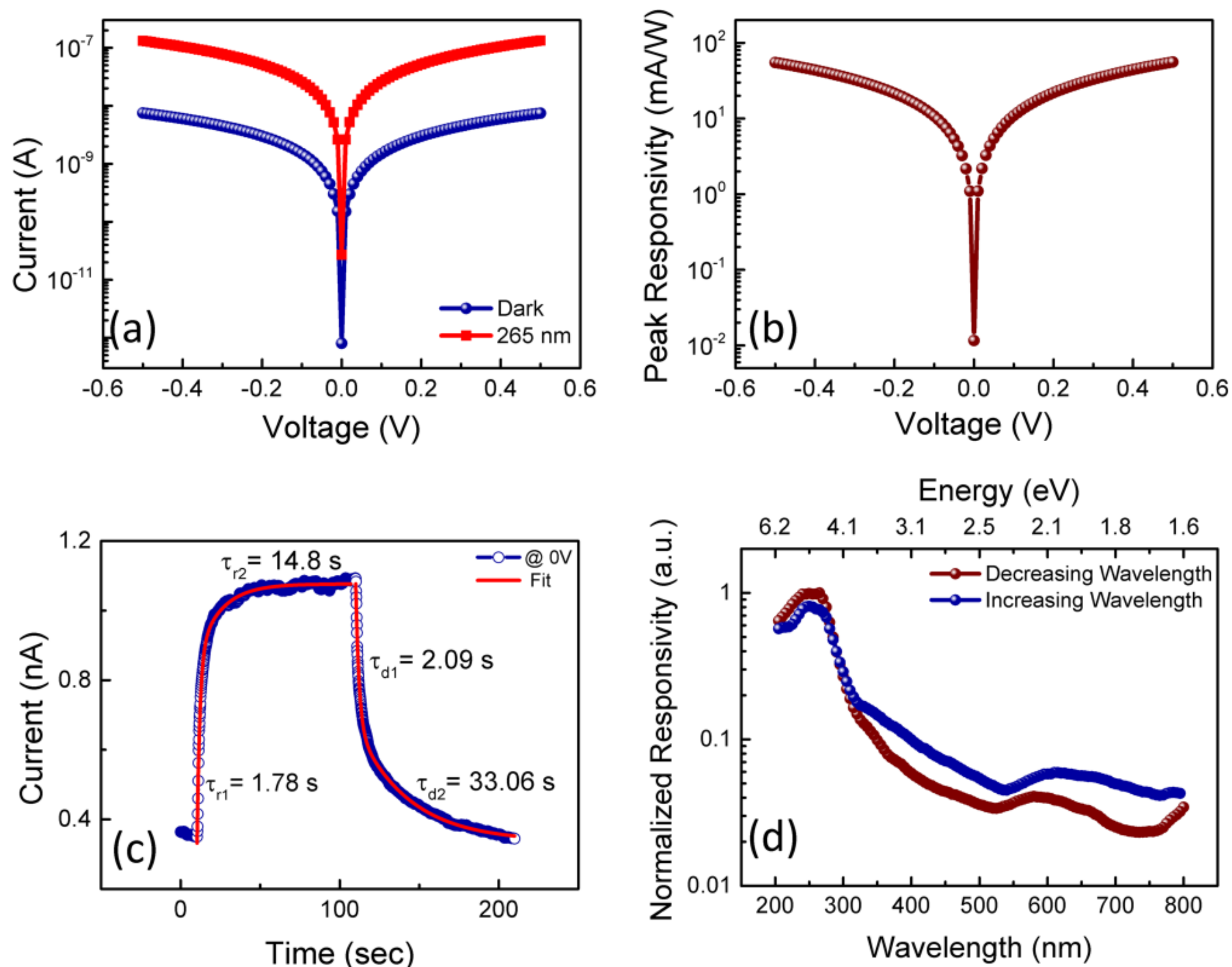

Figure 3. (**a**) Current–voltage measurements under dark and 265 nm wavelength illumination of device, (**b**) peak photoresponsivity, (**c**) time-response measurement at zero bias and (**d**) normalized spectral responsivity.

Material structure	Device structure	Growth technique (Ga_2O_3)	T_{Growth} (°C)	I_{dark} (A)	I_{photo} (A)	P_{opt} (μW/cm²), wavelength	Flexible	Refs.
PEDOT:PSS /Ga_2O_3	p–n	MOCVD	860	~0.1 p	~4 n	1000, 254 nm	No	[55]
PEDOT:PSS /Ga_2O_3 nanowire	p–n	CVD	1120	<0.1 p	–	–, 245 nm	No	[56]
Spiro-MeOTAD/ Ga_2O_3	p–n	MOCVD	860	75 f.	12 n	80, 254 nm	No	[57]
ZnO/Ga_2O_3 microwire	n–n	CVD	1200	~1.0 p	~5.0 n	1670, 251 nm	No	[58]
SiO_2/Ga_2O_3	MOS	MOCVD	735	~2 f.	~0.2 n	30, 254 nm	No	[59]
Ni/Ga_2O_3	Schottky	Sputtering	750	~5 f.	~9 p	150, 254 nm	No	[60]
α/β Ga_2O_3	Phase Junction	Chemical route	700	1.72 n	211 n	3000, 254 nm	No	[61]
Au/Ga_2O_3	MSM	Single crystal	–	0.18 n	2.7 n	1780, 254 nm	No	[62]
Pt/Ga_2O_3	MSM	PLD	550	800 f.	36 p	75, 265 nm	Yes	This work

Table 1. Comparisons of photovoltaic UV-C detectors with different device structures and channel layer growth methods.

is shown in Fig. 3(d). Normalization is carried out by dividing maximum responsivity value to whole spectral responses. The spectral photovoltaic response measurements are performed in the wavelength range of 205 to 800 nm at zero bias. The detector shows the peak photoresponse at 265 nm (4.68 eV) which corresponds to

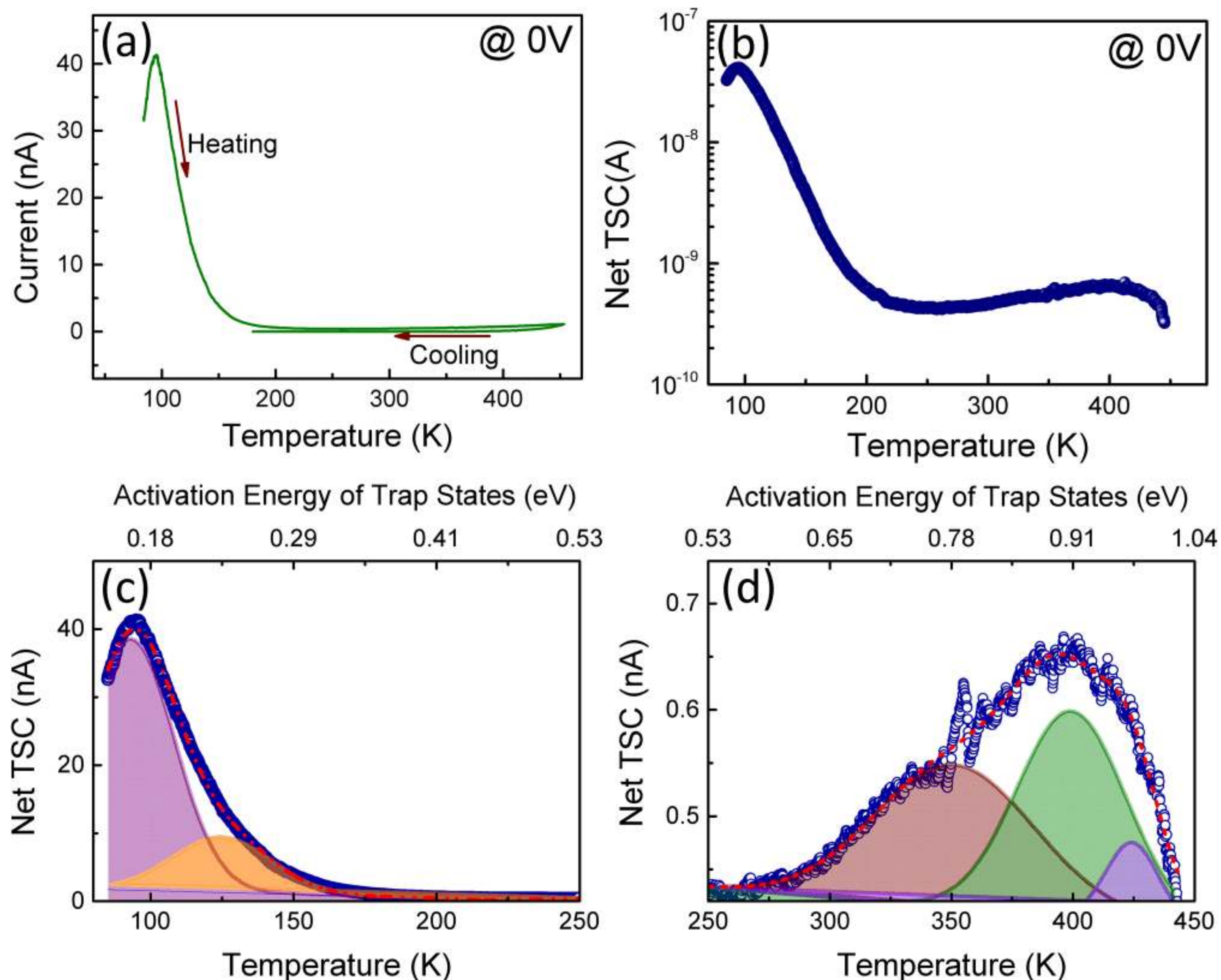

Figure 4. (**a**) TSC curve of the device with 5 K/min heating and cooling rates at zero bias, (**b**) net TSC plot with two broad current peaks (**c**) and (**d**) are the Gaussian fits of both peaks.

the bandgap of β-Ga_2O_3. Thus, the peak photoresponse is observed to lie in the solar-blind region (< 280 nm). Further, the photoresponse at lower wavelengths from 265 to 240 nm remains almost constant and then tends to decrease till 205 nm. In the spectral response curve, various defect bands from 320 to 800 nm are observed. The observation of sub-bandgap absorption is due to optically active recombination centers in β-Ga_2O_3 which tend to generate persistent photocurrent.

Thermally stimulated current (TSC) spectroscopy is employed to explore the role of sub-bandgap states in photocurrent transport. In TSC measurements, all the trap levels are charged optically at a relatively lower temperature to mitigate the thermal emission rate of the carriers from the traps. Thereafter, charge carriers are de-trapped by gradually increasing the temperature at a finite rate under dark conditions and simultaneously recording the stimulated current. Figure 4(a) depicts the thermally stimulated current while heating and cooling at 5 K/min respectively after the charging of trap levels at 85 K. The large difference in the heating and cooling curves is indicative of the presence of traps in the material. The net TSC, which is defined as the total stimulated current minus dark current is shown in Fig. 4(b). In the case of thermally activated electron/hole emission, a particular filled trap starts to emit the charge carriers at a characteristic temperature and later on the emission rate continuously decreases with removal of electron/hole from the trap, generating in this way a current peak. In our particular case, two broad current peaks near about 95 and 400 K have appeared in the net TSC spectra. Both the peaks are fitted with Gaussian to deconvolute the trap states as shown in Fig. 4(c,d) corresponding to peak at 95 and 400 K simultaneously. The first peak is deconvoluted in two peaks centered at 93.3 and 125 K whereas the second peak is deconvoluted into three peaks situated at 351.3, 399.7 and 424.7 K. In the variable heating method of TSC, the activation energy (E_T) of a trap state at a heating rate of γ can be defined as[47]

$$E_T = kT_m ln\left[\frac{T_m^4}{\gamma}\right] + kT_m ln\left(\frac{N_c v_{th} k\sigma_n}{E_T}\right) \quad (4)$$

Traps	Temperature maxima of TSC peak (K)	Activation energy of traps (meV)
E_1	93.3	166
E_2	125.0	234
E_3	351.3	785
E_4	399.7	911
E_5	424.7	977

Table 2. Distribution of bandgap states calculated from thermally stimulated current spectroscopy.

where T_m is the characteristic temperature of TSC peak, ν_{th} is the thermal velocity, N_c is the density of states in the conduction band, σ_n is the capture cross-section of the trap and k is the Boltzmann constant. The second term in Eq. (4) is very small relative to the first term and hence can be neglected[47]. Therefore, Eq. (4) can be approximated for the activation energy of trap state as[47]

$$E_T = kT_m ln\left[\frac{T_m^4}{\gamma}\right] \tag{5}$$

The activation energies of all the traps corresponding to the aforementioned characteristic temperatures are calculated using Eq. (5). The trap states denoted as E_1, E_2, E_3, E_4 and E_5 correspond to the characteristic temperatures of 93.3, 125, 351.3, 399.7 and 424.7 K respectively. The activation energies of all these traps are tabulated in Table 2. These traps have activation energies ranging from 0.1 to 1 eV.

It is observed that E_1 trap having activation energy of 166 meV is the dominant trap among all the five traps. The activation energies corresponding to other traps E_2, E_3, E_4, and E_5 are obtained as 234, 785, 911 and 977 meV respectively. Wang et al. have also investigated the traps in β-Ga_2O_3 thin films which were grown under similar conditions to current work. Traps E_3, E_4 and E_5 exhibited almost same activation energies as reported in the literature[47]. Other than aforementioned traps, Wang et al. also reported the traps with activation energies 0.43, 0.49, 0.52 and 0.54 eV. However, these traps are not observed in the present work which indicative of better crystalline quality of thin film. The energy of E_1 and E_2 levels are relatively shallow and Sn can be the possible origin of these traps. The double donor behavior of Sn is possible due to two different substitutional Ga sites (tetrahedral and octahedral). The behavior of Ge as a double donor with activation energies of 0.18 and 0.21 eV has also been reported using deep level transient spectroscopy (DLTS)[48]. However, further detailed analysis is needed to study the double donor behavior of Ge and Sn in Ga_2O_3. Although both dopants have also been reported as a shallow donor with activation energies less than 50 meV[49]. However, a trap with activation energy of 165 meV was also reported in metal oxide vapor phase epitaxy (MOVPE) grown Ga_2O_3 thin films using deep level noise spectroscopy[50]. The possible origin of this trap is still unknown. Tadjer et al. reported a trap located 0.23 eV below conduction band in halide vapor phase epitaxial Ga_2O_3 which was co-doped by Si and N impurities[51]. Therefore, the E_2 trap of 234 meV may be originated from unintentional nitrogen doping. The E_3 trap having activation energy 785 meV is the most common trap center in Ga_2O_3. It is reported that Fe doping is responsible for this trap[52]. Remaining E_4 and E_5 traps are also common to Ga_2O_3. Irmscher et al. reported that Co impurity may be the origin of these deep traps[48]. On the basis of TSC results, the persistence photocurrent of Ga_2O_3 self-powered photodetectors is due to five trap levels with activation energies ranging from 0.16 to 0.97 eV. Among them, the E_1 trap with activation energy of 166 meV had the dominant contribution in persistence photocurrent.

Further, flexibility tests of photodetectors are performed using the measurement setup shown in Fig. 5(a). The variation of bending radius of the muscovite substrate having 21 mm length was executed from flat condition to 16 mm radius. Figure 5(b) represents the tensile strain in the film with respect to the bending radius. The strain ε induced in the film consisting of thickness t_f can be determined as[53]

$$\varepsilon = \left(\frac{t_f + t_s}{2R_c}\right)\left(\frac{1 + 2\eta + \chi\eta^2}{(1 + \eta)(1 + \chi\eta)}\right) \tag{6}$$

where t_s is the thickness of the substrate, η is defined as t_f/t_s, R_c is the radius of the curvature due to bending and χ is denoted as Y_f/Y_s, Y_f and Y_s are Young's modulus of thin film and substrate respectively. The value of Young's modulus of Ga_2O_3 and muscovite are 261 and 190 GPa, respectively[24,54]. The maximum strain of 0.32% is induced in the film for photoelectrical measurements. Both photocurrent and dark current are recorded with varying bending radii which are shown in Fig. 5(e). The CCD camera images of the mica sheet is also recorded corresponding to flat and bending conditions which are shown in the inset of Fig. 5(c,d). The radius of curvature was 4.99 mm analogous to a 16 mm bending radius. The photocurrent and dark current showed no obvious change and remained almost constant under bending tests which is desirable feature for a flexible photodetector. The excellent performance under bending may be attributed to good structural stability towards mechanical strain of thin film. Other than the structural stability, durability of extremely good metal–semiconductor contacts with mechanical strain resulted in stable dark and photocurrent. In the earlier article, amorphous gallium oxide/muscovite-based photodetectors are reported to possess about one order enhancement in dark as well as photocurrent[7]. Table 3 shows the comparisons of flexible UV-C photodetectors based on gallium oxide thin films. Hence, epitaxial Ga_2O_3/muscovite photodetectors demonstrate much better performance stability towards mechanical flexibility and also has zero power consumption which are very useful properties for e-skins.

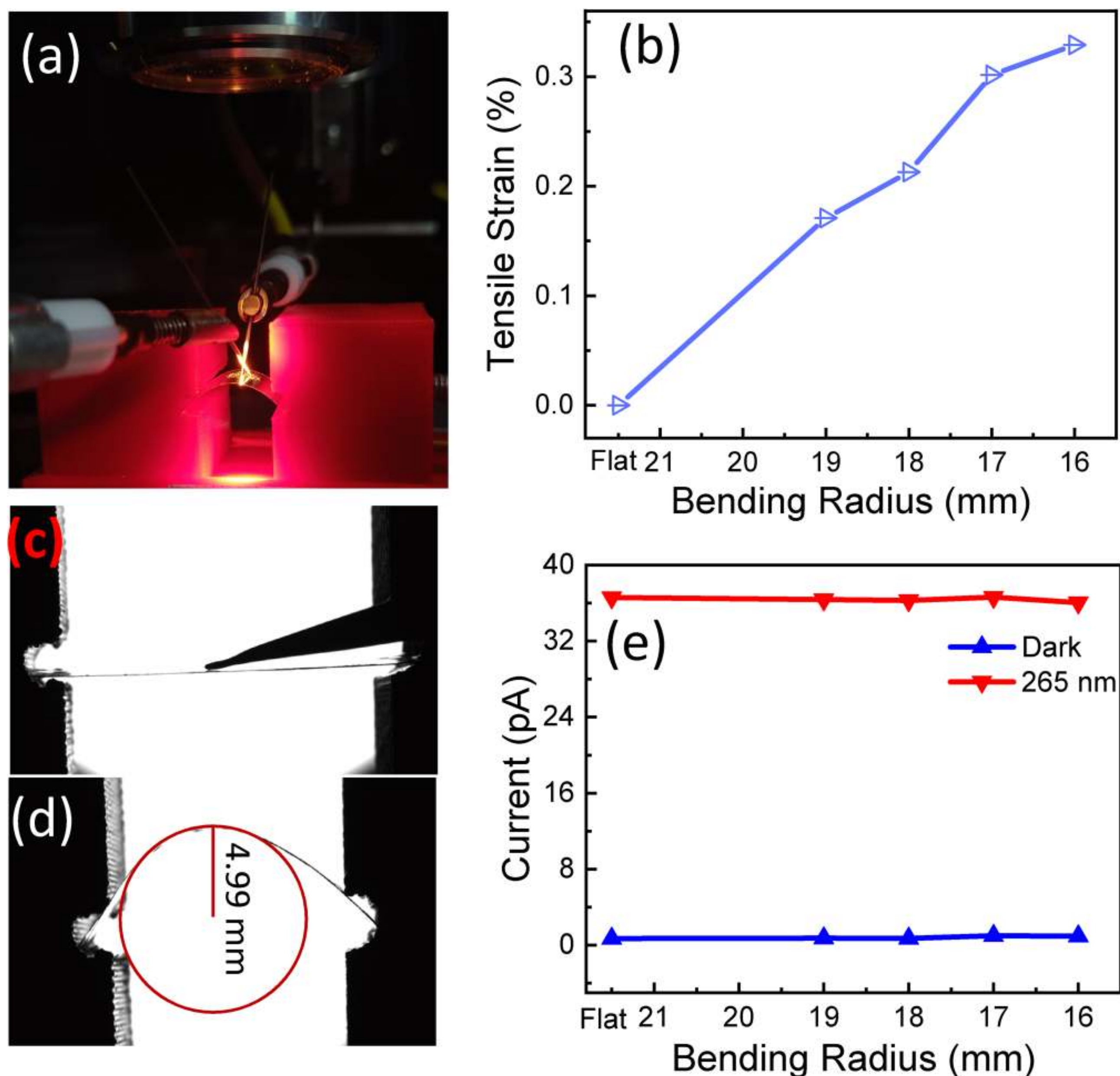

Figure 5. (**a**) Measurement setup for bending tests of the device, (**b**) Tensile strain versus bending radius of the device, (**c**) CCD camera images of a flexible device under flat, (**d**) 16 mm bending radius condition, (**e**) dark and photocurrent of the device at zero bias with bending radius of muscovite.

Heterostructure	Dark current	Photocurrent	Photovoltaic	Bending stability	Refs.
a-GaO/PEN	~ 10^{-13} A @10 V	~ 10^{-8} A	No	No	[23]
a-GaO/PET	~ 10^{-9} A @5 V	~ 10^{-10} A	No	No	[43]
a-GaO/Muscovite	~ 10^{-6} A @5 V	~ 10^{-5} A	No	No	[7]
β-GaO/Muscovite	8×10^{-13} A @0 V	3.6×10^{-11} A	Yes	Yes	This work

Table 3. Comparisons of self-powered and flexible UV-C photodetectors based on Ga_2O_3.

Conclusions

Heteroepitaxy growth of β-$Ga_2O_3(\bar{2}\ 0\ 1)$ on layered muscovite mica substrate has been carried out using pulsed laser deposition. The epitaxial relationship between β-Ga_2O_3 and muscovite is also established using HRXRD and HRTEM. The MSM photodetector made on Ga_2O_3 thin film shows a photovoltaic response corresponding to 265 nm illumination. It is noticed that the photoresponse is influenced by persistence photocurrent. Thermally

stimulated current spectroscopy is employed to investigate trap levels in the devices. The trap with an activation energy of 166 meV is found to dominate the persistence photocurrent among five different trap levels. In addition, the result of bending tests demonstrates excellent stability in photocurrent at zero bias. The obtained results provide a new perspective for photovoltaic and flexible deep UV photodetectors on epitaxial β-Ga_2O_3.

Experimental section

Sample fabrication. The heteroepitaxy of β-Ga_2O_3 on cleaved muscovite (001) is grown using a pulsed laser deposition system (Nobert's electron beam and laser deposition equipment). A KrF excimer laser having 248 nm wavelength is utilized to ablate the tin-doped (1 wt%) gallium oxide target. The laser fluence is kept at 1.5 J/cm^2 with a repetition rate of 5 Hz. The muscovite substrate is placed at a 50 mm distance from the gallium oxide target. The temperature of 550 °C is maintained during the deposition at an oxygen pressure of 5×10^{-3} mbar.

Material characterizations. The X-ray diffraction is acquired with Cu K_α (λ = 1.54 Å) source using a Panalytical Xpert Pro system. The topography of the thin film is mapped using XE-100 Park AFM system. Nanostructural characterization is performed using field emission transmission electron microscope (FE-TEM) system (Jeol, JEM-F200) with a point resolution of about 0.23 nm.

Device fabrication and characterization. The 600 μm long interdigitated electrodes (IDE) at 200 μm spacing are patterned using a metal mask. E-beam evaporation system (Scientific Vacuum System Ltd.) is used to fabricate Pt (20 nm)/Au (80 nm) metal contacts for IDE. Photoelectrical measurements are carried out in an optical cryostat (Janis VPF-700). For Spectral photoresponse distribution, the wavelength of incident light is tuned using a monochromator and Xenon lamp. At the same time, the output current is measured using an electrometer (Keithley, 6517). Further, the photocurrent spectrum is calibrated by power spectrum of the Xenon lamp for photoresponse measurement. The photoresponse distribution is normalized with respect to the maximum response value.

Thermally stimulated current measurements. For the TSC experiment, the device is cooled down from room temperature to 85 K under the dark conditions in a cryostat. The trap filling in Ga_2O_3 is performed under 265 nm wavelength illumination at 85 K. To ensure the better trap filling, the device is illuminated at zero bias for 20 min with 20 μW/cm^2 power density of 265 nm light. Further, illumination is turned off and charge carriers were de-trapped by heating the device up to 450 K with a constant heating rate of 5 K/min. Simultaneously, the thermally stimulated current is recorded with increasing temperature. The dark current measurements are also conducted with temperature to ensure the net TSC in the device.

Data availability

The raw/processed data required to reproduce these findings cannot be shared at this time as the data also forms part of an ongoing study. In future, it will be provided on request by corresponding author.

Received: 31 March 2020; Accepted: 4 May 2020
Published online: 30 September 2020

References

1. Xu, K. C., Lu, Y. Y. & Takei, K. Multifunctional skin-inspired flexible sensor systems for wearable electronics. *Adv. Mater. Technol.* **4**(3), 1800628 (2019).
2. Núñez, C. G., Navaraj, W. T., Polat, E. O. & Dahiya, R. Energy-autonomous, flexible, and transparent tactile skin. *Adv. Funct. Mater.* **27**, 1606287 (2017).
3. Le, V.-Q. *et al.* Van der Waals heteroepitaxial AZO/NiO/AZO/muscovite (ANA/muscovite) transparent flexible memristor. *Nano Energy* **56**, 322–329 (2019).
4. Georgiou, T. *et al.* Vertical field-effect transistor based on graphene–WS_2 heterostructures for flexible and transparent electronics. *Nat. Nanotechnol.* **8**, 100–103 (2013).
5. Nomura, K. *et al.* Room-temperature fabrication of transparent flexible thin-film transistors using amorphous oxide semiconductors. *Nature* **432**, 488–492 (2004).
6. Zheng, Z. Q., Yao, J. D. & Yang, G. W. Growth of centimeter-scale high-quality In_2Se_3 films for transparent, flexible and high performance photodetectors. *J. Mater. Chem. C* **4**, 8094–8103 (2016).
7. Tak, B. R., Gupta, V., Kapoor, A. K., Chu, Y.-H. & Singh, R. Wearable gallium oxide solar-blind photodetectors on muscovite mica having ultrahigh photoresponsivity and detectivity with added high-temperature functionalities. *ACS Appl. Electron. Mater.* **1**, 2463–2470 (2019).
8. Zhou, L. *et al.* High-performance flexible organic light-emitting diodes using embedded silver network transparent electrodes. *ACS Nano* **8**, 12796–12805 (2014).
9. Sarwar, M. S. *et al.* Bend, stretch, and touch: Locating a finger on an actively deformed transparent sensor array. *Sci. Adv.* **3**, e1602200 (2017).
10. Retamal, J. R. D., Ho, C., Tsai, K., Ke, J. & He, J. Self-organized Al nanotip electrodes for achieving ultralow-power and error-free memory. *IEEE Trans. Electron. Dev.* **66**, 938–943 (2019).
11. NK Wood Research Global Flexible Electronics Market Forecast 2018–2026, https://www.inkwoodresearch.com/reports/flexible-electronics-market/#report-summary (2018).
12. Guo, Y. B., Li, Y. G., Zhang, Q. H. & Wang, H. Z. Self-powered multifunctional UV and IR photodetector as an artificial electronic eye. *J. Mater. Chem. C* **5**, 1436–1442 (2017).
13. The International Commission on Non-Ionizing Radiaton Protection. Guidelines on limits of exposure to ultraviolet radiation of wavelengths between 180 and 400 nm (incoherent optical radiation). *Health Phys.* **87**, 171–186 (2004).
14. Tak, B. R. *et al.* High-temperature photocurrent mechanism of β-Ga_2O_3 based metal-semiconductor-metal solar-blind photodetectors. *J. Appl. Phys.* **125**, 144501 (2019).

15. Tak, B. R. *et al.* Point defects induced work function modulation of beta- Ga_2O_3. *Appl. Surf. Sci.* **465**, 973–978 (2019).
16. Chen, H., Liu, H., Zhang, Z., Hu, K. & Fang, X. Nanostructured photodetectors: from ultraviolet to terahertz. *Adv. Mater.* **28**, 403–433 (2016).
17. Lou, Z., Li, L., Wang, L. & Shen, G. *Recent progress of self-powered sensing systems for wearable electronics.* **13**, 1701791 (2017).
18. Tian, W., Wang, Y., Chen, L. & Li, L. Self-Powered Nanoscale Photodetectors. *Small* **13**, 1701848 (2017).
19. Yang, W. *et al.* Silicon-compatible photodetectors: trends to monolithically integrate photosensors with chip technology. *Adv. Func. Mater.* **29**, 1808182 (2019).
20. Zhang, Y. *et al.* Self-powered dual-color UV–green photodetectors based on SnO_2 millimeter wire and microwires/$CsPbBr_3$ particle heterojunctions. *J. Phys. Chem. Lett.* **10**, 836–841 (2019).
21. Lu, S. *et al.* Piezotronic interface engineering on ZnO/Au-based Schottky junction for enhanced photoresponse of a flexible self-powered UV detector. *ACS Appl. Mater. Int.* **6**, 14116–14122 (2014).
22. Shi, X. *et al.* A flexible GaN nanowire array-based schottky-type visible light sensor with strain-enhanced photoresponsivity. *Adv. Electron. Mater.* **1**, 1500169 (2015).
23. Cui, S. J., Mei, Z. X., Zhang, Y. H., Liang, H. L. & Du, X. L. Room-temperature fabricated amorphous Ga_2O_3 high-response-speed solar-blind photodetector on rigid and flexible substrates. *Adv. Opt. Mater.* **5**, 1700454 (2017).
24. Bitla, Y. & Chu, Y.-H. MICAtronics: a new platform for flexible X-tronics. *FlatChem* **3**, 26–42 (2017).
25. Zhang, X. T., He, Y. D., Li, R. J., Dong, H. L. & Hu, W. P. 2D mica crystal as electret in organic field-effect transistors for multistate memory. *Adv. Mater.* **28**, 3755–3760 (2016).
26. Skin to e-skin. *Nat. Nanotechnol.* **12**, 1017–1017 (2017).
27. Koma, A. & Yoshimura, K. Ultrasharp interfaces grown with Van der Waals epitaxy. *Surf. Sci.* **174**, 556–560 (1986).
28. Koma, A. Van der Waals epitaxy—a new epitaxial growth method for a highly lattice-mismatched system. *Thin Solid Films* **216**, 72–76 (1992).
29. Wu, P.-C. *et al.* Epitaxial Yttria-stabilized zirconia on muscovite for flexible transparent ionic conductors. *ACS Appl. Nano Mater.* **1**, 6890–6896 (2018).
30. Li, C.-I. *et al.* van der Waal epitaxy of flexible and transparent VO2 film on muscovite. *Chem. Mater.* **28**, 3914–3919 (2016).
31. Ma, C.-H. *et al.* Van der Waals epitaxy of functional MoO_2 film on mica for flexible electronics. *Appl. Phys. Lett.* **108**, 253104 (2016).
32. Liu, H.-J. *et al.* Flexible heteroepitaxy of $CoFe_2O_4$/muscovite bimorph with large magnetostriction. *Acs Appl. Mater. Int.* **9**, 7297–7304 (2017).
33. Wu, P.-C. *et al.* Heteroepitaxy of Fe_3O_4/Muscovite: a new perspective for flexible spintronics. *ACS Appl. Mater. Int.* **8**, 33794–33801 (2016).
34. Xu, J. J., Zheng, W. & Huang, F. Gallium oxide solar-blind ultraviolet photodetectors: a review. *J. Mater. Chem. C* **7**, 8753–8770 (2019).
35. Chen, X. H., Ren, F. F., Gu, S. L. & Ye, J. D. Review of gallium-oxide-based solar-blind ultraviolet photodetectors. *Photon. Res.* **7**, 381–415 (2019).
36. Hou, M. M., So, H. Y., Suria, A. J., Yalamarthy, A. S. & Senesky, D. G. Suppression of persistent photoconductivity in AlGaN/GaN ultraviolet photodetectors using in situ heating. *IEEE Electr. Device L* **38**, 56–59 (2017).
37. Mouillet, R. *et al.* Photoresponse and defect levels of AlGaN/GaN heterobipolar phototransistor grown on low-temperature AlN interlayer. *Jpn. J. Appl. Phys. Part-2. Lett. Express Lett.* **40**, 498–501 (2001).
38. Xie, F. *et al.* Large-area solar-blind AlGaN-based MSM photodetectors with ultra-low dark current. *Electron. Lett.* **47**, 930–931 (2011).
39. Xie, F. *et al.* Ultra-low dark current AlGaN-based solar-blind metal-semiconductor-metal photodetectors for high-temperature applications. *IEEE Sens. J.* **12**, 2086–2090 (2012).
40. Garg, M., Tak, B. R., Rao, V. R. & Singh, R. Giant UV photoresponse of GaN-based photodetectors by surface modification using phenol-functionalized porphyrin organic molecules. *ACS Appl. Mater. Int.* **11**, 12017–12026 (2019).
41. Chen, X., Ren, F.-F., Ye, J. & Gu, S. Gallium oxide-based solar-blind ultraviolet photodetectors. *Semicond. Sci. Technol.* **35**, 023001 (2020).
42. Hirano, A. *et al.* Demonstration of flame detection in room light background by solar-blind AlGaN PIN photodiode. *Physica Status Solidi (a)* **188**, 293 (2001).
43. Kumar, N., Arora, K. & Kumar, M. High performance, flexible and room temperature grown amorphous Ga_2O_3 solar-blind photodetector with amorphous indium-zinc-oxide transparent conducting electrodes. *J. Phys. D-Appl. Phys.* **52**, 335103 (2019).
44. 44Hao, S. J. *et al.* Growth and characterization of β- Ga_2O_3 thin films on different substrates. **125**, 105701, (2019).
45. Pratiyush, A. S. *et al.* High responsivity in molecular beam epitaxy grown beta- Ga_2O_3 metal semiconductor metal solar blind deep-UV photodetector. *Appl. Phys. Lett.* **110**, 221107 (2017).
46. Tak, B. R., Garg, M., Kumar, A., Gupta, V. & Singh, R. Gamma irradiation effect on performance of β-Ga_2O_3 metal-semiconductor-metal solar-blind photodetectors for space applications. *ECS J. Solid State Sci. Technol.* **8**, Q3149–Q3153 (2019).
47. Wang, B. G., Look, D. & Leedy, K. Deep level defects in beta- Ga_2O_3 pulsed laser deposited thin films and Czochralski-grown bulk single crystals by thermally stimulated techniques. *J. Appl. Phys.* **125**, 105103 (2019).
48. Farzana, E., Ahmadi, E., Speck, J. S., Arehart, A. R. & Ringel, S. A. Deep level defects in Ge-doped (010) beta- Ga_2O_3 layers grown by plasma-assisted molecular beam epitaxy. *J. Appl. Phys.* **123**, 161410 (2018).
49. Tadjer, M. J. *et al.* Review-Theory and Characterization of Doping and Defects in beta- Ga_2O_3. *ECS J. Solid State Sci.* **8**, Q3187–Q3194 (2019).
50. Golz, C. *et al.* Deep-level noise characterization of MOVPE-grown β- Ga_2O_3. *Appl. Phys. Lett.* **115**, 133504 (2019).
51. Tadjer, M. J. *et al.* High resistivity halide vapor phase homoepitaxial β- Ga_2O_3 films co-doped by silicon and nitrogen. *Appl. Phys. Lett.* **113**, 192102 (2018).
52. Neal, A. T. *et al.* Donors and deep acceptors in β- Ga_2O_3. *Appl. Phys. Lett.* **113**, 062101 (2018).
53. Bitla, Y. *et al.* Oxide heteroepitaxy for flexible optoelectronics. *ACS Appl. Mater. Int.* **8**, 32401–32407 (2016).
54. Zheng, X.-Q. *et al.* Beta gallium oxide (β- Ga_2O_3) nanoelectromechanical transducer for dual-modality solar-blind ultraviolet light detection. *APL Mater.* **7**, 022523 (2019).
55. Li, S. *et al.* A self-powered solar-blind photodetector with large Voc enhancing performance based on the PEDOT:PSS/Ga_2O_3 organic–inorganic hybrid heterojunction. *J. Mater. Chem. C* **8**, 1292–1300 (2020).
56. Wang, H. *et al.* High responsivity and high rejection ratio of self-powered solar-blind ultraviolet photodetector based on PEDOT:PSS/β-Ga_2O_3 organic/inorganic p–n junction. *J. Phys. Chem. Lett.* **10**, 6850–6856 (2019).
57. Yan, Z. *et al.* High sensitivity and fast response self-powered solar-blind ultraviolet photodetector with a β-Ga_2O_3/spiro-MeOTAD p–n heterojunction. *J. Mater. Chem. C* **8**, 4502–4509 (2020).
58. Zhao, B. *et al.* An ultrahigh responsivity (9.7 mA W-1) self-powered solar-blind photodetector based on individual ZnO–Ga_2O_3 heterostructures. *Adv. Funct. Mater.* **27**, 1700264 (2017).
59. Liu, Z. *et al.* Construction of a β-Ga_2O_3 -based metal–oxide–semiconductor-structured photodiode for high-performance dual-mode solar-blind detector applications. *J. Mater. Chem. C* **8**, 5071–5081 (2020).
60. Liu, Z. *et al.* A high-performance ultraviolet solar-blind photodetector based on a β- Ga_2O_3 Schottky photodiode. *J. Mater. Chem. C* **7**, 13920–13929 (2019).

61. Wu, C. *et al.* Vertical α/β-Ga_2O_3 phase junction nanorods array with graphene-silver nanowire hybrid conductive electrode for high-performance self-powered solar-blind photodetectors. *Mater. Today Phys.* **12**, 100193 (2020).
62. Dong, L. P. *et al.* Self-powered MSM deep-ultraviolet beta-Ga_2O_3 photodetector realized by an asymmetrical pair of Schottky contacts. *Opt. Mater. Express* **9**, 1191–1199 (2019).

Acknowledgements

B. R. Tak acknowledges the Department of Science and Technology (DST), India and British Council, UK for awarding short-term research internship under the Newton-Bhabha Ph.D. programme (Award No- DST/INSPIRE/NBHF/2018/1) at the University of Warwick, UK to conduct this work. B.R. Tak also likes to thank DST India for providing INSPIRE fellowship during the Ph.D. program. Nanoscale Research Facility at IIT Delhi is gratefully acknowledged for UV photodetector characterization.

Author contributions

B.R.T.: Growth, characterizations, analysis and writing. M.-M.Y.: TSC data analysis, review and editing. Y.-H.L.: TEM measurements and analysis, review. Y.-H.C.: Review and editing. M.A.: TSC data analysis, supervision, review and editing. R.S.: Conceptualization, supervision, review and editing.

Funding

This research was funded by Department of Science and Technology (DST), India and British Council, UK under the Newton-Bhabha Ph.D. programme (Award No- DST/INSPIRE/NBHF/2018/1).

Competing interests

The authors declare no competing interests.

Additional information

Supplementary information is available for this paper at https://doi.org/10.1038/s41598-020-73112-1.

Correspondence and requests for materials should be addressed to B.R.T.

Reprints and permissions information is available at www.nature.com/reprints.

Publisher's note Springer Nature remains neutral with regard to jurisdictional claims in published maps and institutional affiliations.

Open Access This article is licensed under a Creative Commons Attribution 4.0 International License, which permits use, sharing, adaptation, distribution and reproduction in any medium or format, as long as you give appropriate credit to the original author(s) and the source, provide a link to the Creative Commons licence, and indicate if changes were made. The images or other third party material in this article are included in the article's Creative Commons licence, unless indicated otherwise in a credit line to the material. If material is not included in the article's Creative Commons licence and your intended use is not permitted by statutory regulation or exceeds the permitted use, you will need to obtain permission directly from the copyright holder. To view a copy of this licence, visit http://creativecommons.org/licenses/by/4.0/.

© The Author(s) 2020